**Radiolysis-Driven Evolution of Gold Nanostructures – Model Verification by Scale Bridging *in situ* Liquid-Phase Transmission Electron Microscopy and X-ray Diffraction**

*Birk Fritsch*, Tobias Zech, Mark Bruns, Andreas Körner, Saba Khadivianazar, Mingjian Wu, Neda Zargar Talebi, Sannakaisa Virtanen, Tobias Unruh, Michael P.M. Jank, Erdmann Spiecker, Andreas Hutzler**

B. Fritsch, S. Khadivianazar, N. Zargar Talebi, Dr. M. P. M. Jank, Andreas Hutzler
Friedrich-Alexander-Universität Erlangen-Nürnberg
Department of Electrical, Electronic and Communication Engineering
Electron Devices (LEB)
Cauerstraße 6, 91058 Erlangen, Germany
E-mail: birk.fritsch@fau.de

B. Fritsch, Dr. M. Wu, Prof. E. Spiecker
Friedrich-Alexander-Universität Erlangen-Nürnberg
Department of Materials Science and Engineering
Institute of Micro- and Nanostructure Research (IMN) and Center for Nanoanalysis and Electron Microscopy (CENEM)
Cauerstraße 3, 91058 Erlangen, Germany

T. Zech, Prof. T. Unruh
Friedrich-Alexander-Universität Erlangen-Nürnberg
Department of Physics
Institute of Condensed Matter Physics and Institute for Crystallography and Structural Physics (ICSP), Institute of Micro- and Nanostructure Research (IMN), and Center for Nanoanalysis and Electron Microscopy (CENEM)
Staudtstraße 3, 91058 Erlangen, Germany
Cauerstraße 3, 91058 Erlangen, Germany

M. Bruns, Prof. S. Virtanen
Friedrich-Alexander-Universität Erlangen-Nürnberg
Department of Materials Science and Engineering
Surface Science and Corrosion (LKO)
Martensstraße 7, 91058 Erlangen, Germany

A. Körner, Dr. A. Hutzler,
Forschungszentrum Jülich GmbH,
Helmholtz Institute Erlangen-Nürnberg for Renewable Energy (IEK-11),
Cauerstraße 1, 91058 Erlangen, Germany
E-mail: a.hutzler@fz-juelich.de

Dr. M. P. M. Jank
Fraunhofer Institute for Integrated Systems and Device Technology IISB
Schottkystraße 10, 91058 Erlangen, Germany

Keywords:
kinetic modelling, radiolysis, gold nanoparticles, particle growth, oxidative etching, critical radius, liquid cell transmission electron microscopy

Formation and degradation of gold nanostructures in tetrachloroauric acid ($HAuCl_4$) is comprehensively investigated *via in situ* liquid-phase transmission electron microscopy (LP-TEM). By introducing a novel technique to simulate arbitrary kinetic models for radiochemistry, we provide a holistic understanding of reaction mechanisms in irradiated $HAuCl_4$ solutions, allowing for quantitative prediction and tailoring of redox processes in LP-TEM experiments. It is demonstrated that no experimentally relevant threshold for gold reduction during LP-TEM exists and that radiation-induced metal-ion reduction is relevant even for experiments utilizing X-rays such as X-ray diffraction (XRD). Furthermore, we unveil that oxidative etching of gold nanoparticles depends on both, precursor concentration, and dose rate. This dependency is harnessed to probe the electron beam-induced shift in the Gibbs free energy landscape by analyzing the critical radius of gold nanoparticles.

## 1. Introduction

Liquid-phase transmission electron microscopy (LP-TEM) emerged as a cutting-edge *in situ* technique for investigation of processes at the nanoscale.[1,2] Particularly in the fields of catalysis,[3,4] energy materials and storage,[5–7] soft-matter studies,[8,9] or virology,[10,11] LP-TEM has been enabling unprecedented insights into fundamental processes, such as non-classical crystallization pathways[12–14] and nanostructure self-assembly.[15]

However, inherent inelastic electron-matter interactions influence the Gibbs free energy landscape.[16,17] To enable LP-TEM becoming a standard characterization method this needs to be accounted for appropriately. Besides electron beam-induced heating,[18,19] radiolysis is a crucial factor during LP-TEM,[20–23] even when radical scavengers are utilized[24,25] or radiolytic shielding *via* graphene membranes is harnessed.[26,27] Moreover, radiochemistry has been identified as a prime driving force to study both reductive formation,[28–30] and oxidative etching[31–35] of metallic nanostructures. Operating between the poles of mitigation and utilization of radiation effects is not limited to LP-TEM but is relevant for many experiments

investigating structures or processes in liquids utilizing ionizing radiation.[36] Thus, understanding the radiochemistry is *the* key for appropriate experimental design and interpretation.

However, most LP-TEM studies solely rely on an incomplete description of the chemical environment, ignoring the intra- and interplay of complete clusters of chemical species. For example, investigations of gold nanoparticle evolution in aqueous tetrachloroauric acid ($HAuCl_4$) solution, one of the most frequently used model systems in LP-TEM,[12,28,32,37–46] mainly rely on the radiochemistry of pure (and partially even deaerated) water.[21] More accurate descriptions are sparse and only describe gold precursor reduction[24,38] or the radical chemistry of aqueous chloride solutions.[37]

In this study, we introduce a novel approach to translate chemical reaction sets into kinetic models, drastically simplifying and therefore allowing for a completion of the accurate description of the complex solution chemistry during LP-TEM. We demonstrate the full potential of this approach by providing a comprehensive description of the radiochemistry of aqueous $HAuCl_4$ solutions, unveiling that the interplay between aqueous, gold-, and chlorine-containing species is crucial for an appropriate description of the solution chemistry. By using LP-TEM and liquid cell X-ray diffraction (XRD), we show that it is essential to consider the impact of ionizing radiation even for experiments with 'low dose rate' irradiation techniques. Furthermore, we reveal how the initial $HAuCl_4$ concentration determines the redox-interplay during LP-TEM and probe the impact on the Gibbs free energy landscape by investigating the inherent stability of gold nanoparticles in oxidative environments.

## 2. Tool for automated radiolysis simulations

Radiochemistry inside a homogeneous volume element of a liquid phase irradiated with a steady electron beam is simulated under the assumption of an isotropic distribution of all contributing species. In this voxel, the chemical interplay is described by a set of coupled

ordinary differential equations (ODEs)[21], describing the evolution of concentration *c* over time *t* of a reactant *i* depending on the concentrations of different reactants *l* and *n* (see the supporting information S1.1 for details):

$$\frac{\partial c_i}{\partial t} = \frac{\rho}{F}\psi G_i + \sum_j k_j \left(\prod_l c_l\right) - \sum_{m \neq j} k_m \left(\prod_n c_n\right) \quad (1)$$

Here, $\rho$ denotes the liquid density, $F$ the Faraday constant, $\psi$ the dose rate in Gy·s$^{-1}$, $G_i$ the generation value ($g$-value) of species $i$, and $k_j$, $k_m$ the kinetic constant of the reaction $j$ or $m$. In a homogeneously irradiated liquid volume, a quasi-closed system can emerge where diffusion of chemical species towards non-irradiated volumes is negligible.[32,47]

In the past, radiolysis simulations have been achieved by manually creating the set of ordinary differential equations to solve equation (1). This is a cumbersome and highly complicated process, prone to errors which are hard to detect. Consequently, extensions of the reaction set comprising pure water are sparse and mostly limited to comparatively few additional reactions. To overcome these obstacles, we provide a newly developed routine solely relying on open-source software. The code based on Python 3.7, NumPy,[48] Matplotlib,[49] pandas,[50] and SciPy[51] accepts a plain-text file of the chemical reaction set as input and automatically generates the corresponding matrix of coupled differential equations. Its outcome has been validated against the MATLAB implementation of the reaction set of Schneider *et al.*,[21] revealing excellent agreement in both temporal (***Figure* S1*(a)***) and steady-state evolution (***Figure* S1*(b)***). The flowchart is sketched in ***Figure 1(a).***

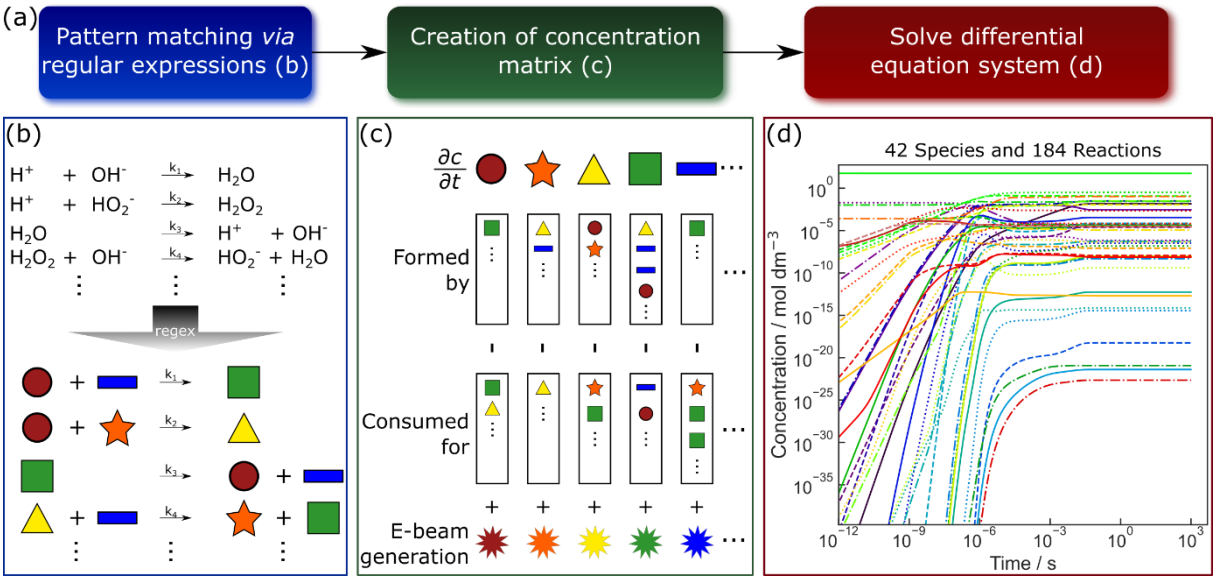


**Figure 1:** (a) Workflow of the generalized simulation tool. (b) Illustration of pattern matching using regular expressions (regex) for generating a set of coupled differential equations (c), which are then solved numerically (d).

***Figure 1(b)*** illustrates that this is achieved by using natural language processing *via* regular expressions (regex). Next, the reaction set is translated into a matrix to provide suitable input for a numerical ODE-solver (***Figure 1(c)***).

An exemplary output of the solver is shown in ***Figure 1(d)*** for a comprehensive reaction set describing the evolvement and equilibration of relevant constituents in an irradiated aqueous $HAuCl_4$ solution. It consists of 42 chemical species distributed over 184 reactions (see the supporting information for details,[21,37,38,52–66] including an enlarged and annotated version of the plot depicted in ***Figure 1(d)*** (***Figure* S*3***)). ***Figure* S*4*** depicts the set based on graph theory,[67,68] revealing that the simulated steady-state concentrations of the species do not necessarily coincide with their importance within the reaction set (c.f. ***Figure S5***). A tabular representation and further information can be found in the supporting information (**Table S*2***, and **S1 Radiolysis**).

## 3. Results and discussions

***Figure 2*** displays the steady-state concentrations of the main non-aqueous radiolysis products of 20 mM $HAuCl_4$ solution. At dose rates relevant to LP-TEM, steady-state concentrations are approached within a few milliseconds, exemplarily shown in ***Figure 1(d)***. Reactants are defined as a main product if their steady-state concentration exceeds 1% of the initial $HAuCl_4$ concentration at least once in the dose rate interval of irradiation. It is evident that not only a single but two Au-containing species fall into this category, namely elementary Au and a gold dimer, $Au_2Cl_6^{2-}$. The main amount of chlorine, in turn, is distributed into $Cl^-$, molecular HCl, and $Au_2Cl_6^{2-}$. The corresponding logarithmically scaled plot including aqueous species is displayed in ***Figure S7***.

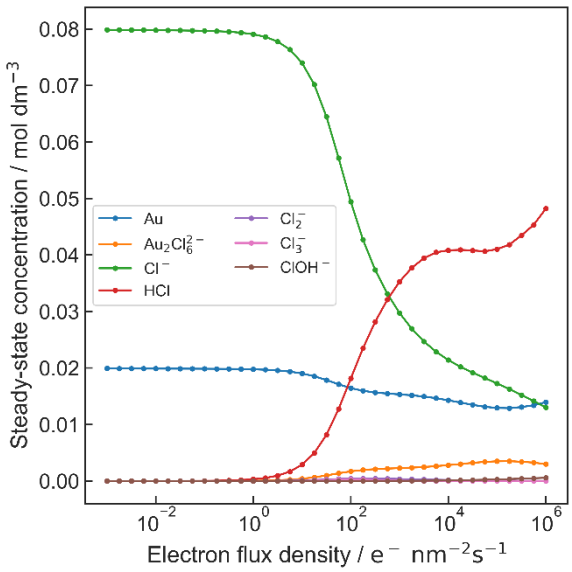


**Figure 2**: Non-aqueous species exceeding 1% of the initial $HAuCl_4$ concentration of 20 mM. A logarithmically-scaled plot including aqueous species is given in ***Figure S7***.

$Cl^-$ and Au appear to be the main products at low electron flux densities. HCl dominates the chlorine distribution at high electron flux densities, despite its strong dissociation behavior. Albeit most Au remains in a pristine state, a significant increase in the concentration of $Au_2Cl_6^{2-}$ with ascending electron flux density is evident.

These outcomes are particularly relevant as their consequences are accessible experimentally:

- Gold ions will be reduced to elementary gold at low electron flux densities by irradiation.

- HCl and $Au_2Cl_6^{2-}$ exhibit high vapor pressures and are expected to appear in gaseous phases.
- Oxidative etching of gold nanostructures is fostered at high electron flux densities.

These conclusions are evaluated in the following.

*3.1 Dose rate requirements for gold nanostructure growth*

The most prominent consequence of irradiating $HAuCl_4$-solutions is the reduction of gold-containing species to elementary Au, which agglomerates and forms crystalline structures easily detectable in TEM. For this mechanism, an electron flux density exceeding an estimated threshold between $2 \cdot 10^3$ and $3 \cdot 10^3$ $e^-$ $(nm^2s)^{-1}$ was concluded previously.[37,38]

However, our simulation results (***Figure 2***) do not indicate a threshold existing for irradiation of a 20 mM $HAuCl_4$ solution, the same specimen investigated by Park *et al.*.[37] A respective experiment, demonstrated in ***Figure S8***, displays a growth event of a gold nanostructure at 540 $e^-$ $(nm^2s)^{-1}$. The growth rate decreased over time, suggesting the convergence against a steady-state condition. This observation indicates the existence of "sub-threshold" gold reduction.

To further investigate this discrepancy, kinetic simulations have been performed for varying initial $HAuCl_4$ concentrations and electron flux densities (***Figure 3***). Simulation results are indicated by a grid comprising of open gray rectangles. Parameters in between are interpolated cubically. The initial $HAuCl_4$ concentration is the logical benchmark to characterize the system because it is not only an experimentally accessible parameter but also summarizes the initial pH value and the total amount of chlorine and gold present.

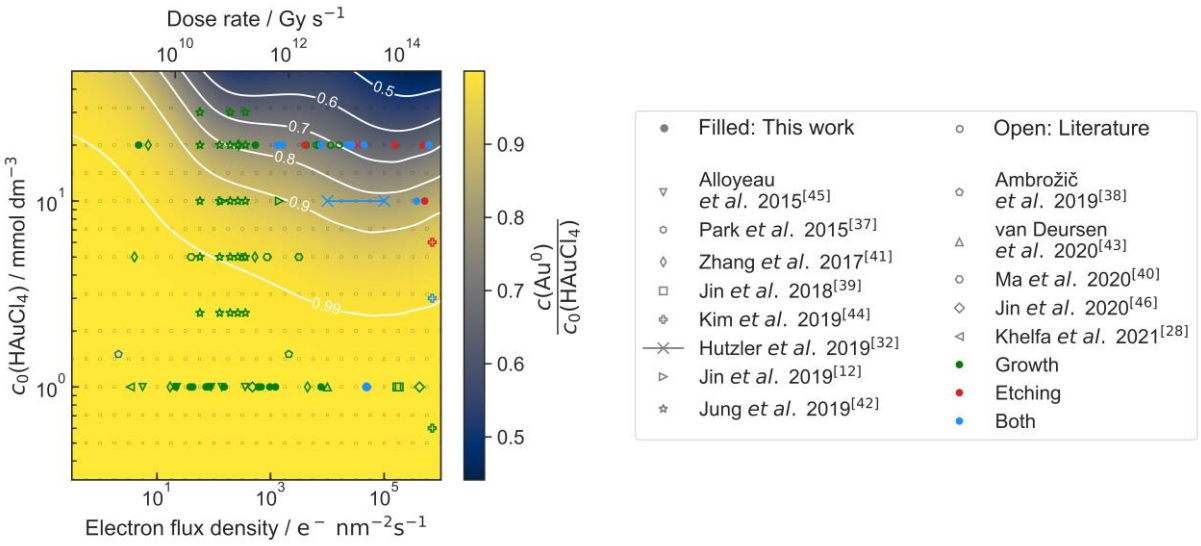


**Figure 3**: The equilibrium mole fraction of $Au^0$ is mapped against electron flux density and initial concentration of $HAuCl_4$. Gray open rectangles denote simulated values. The data in-between is interpolated. Note that no extrapolation is performed. Level lines are shown in white. Green, red, and blue marks account for experimental observations relating to growth, etching, or both (simultaneously or subsequently), respectively. Unfilled marks annotate literature reports of radiolytic $HAuCl_4$-reduction in aqueous LP-TEM experiments, while filled marks represent findings acquired during this work.

The resulting relative amount of gold reduced to $Au^0$ is mapped in ***Figure 3***. It is evident that the (almost) complete reduction of $AuCl_4^-$ to $Au^0$ holds for all concentrations investigated at low dose rates and even at low initial $HAuCl_4$ concentrations for all electron flux densities under investigation.

The existence of an electron-flux threshold required for gold-particle formation is also not evident when surveying LP-TEM literature available elucidating gold reduction from pristine $HAuCl_4$ solution[28,32,37–46]. In ***Figure 3***, an overview of experiments reported in literature dealing with the formation of solid-state gold in LP-TEM experiments is provided.

In this work, the dose rate is calculated for an electron energy of 300 kV and for a liquid film with a constant thickness of about 100 nm to describe our experiments performed in graphene-supported microwell liquid cells (GSMLCs).[47,69] Naturally, this cannot be matched perfectly with the broad range of experiments reported in the literature. Therefore, the literature comparison shown cannot describe the gold ratio quantitatively but provides an orientation in

terms of orders of magnitude, as variations induced by alterations in energy of the primary electrons and liquid thickness are small compared to the regarded scales.

Nonetheless, ***Figure 3*** clearly reveals that any considered thresholds are undercut frequently. This is why in some cases, gold nanostructure formation is regarded as a benchmark experiment for successfully sealed liquid cells.[70,71]

To investigate the existence of an experimentally relevant threshold for gold precipitation in $HAuCl_4$-solution under exposure with ionizing irradiation, a 20 mM $HAuCl_4$-solution was exposed to a Cu $K_\alpha$ X-ray beam. With roughly 1 Gy $s^{-1}$, this experiment was performed at a dose rate of about nine orders of magnitude below the lowest dose rate depicted in ***Figure 3***.

Optical micrographs (***Figure 4*****(a)**) reveal precipitation consisting of microstructures, which did not emerge in the corresponding reference experiment without X-ray exposure. As shown in the inset, a notable amount of precipitation forms platelet structures with the typical three- or sixfold symmetry expected from fcc-crystallites. ***Figure S9(a)*** shows that the precipitation is visible by the naked eye. The lattice planes of the particle layer were investigated *ex situ* using XRD to characterize the crystal structures further. As demonstrated in **Figure S*9(b)***, the Bragg peaks match well to lattice planes of gold.[72]

Another ultra-low dose rate-mediated reductive gold synthesis was conducted for 42 h while repeatedly performing *in situ* XRD scans in 2 h intervals with a temporal resolution of 20 min (***Figure 4(b)***). An apparent increase in diffraction peak intensity with continuous irradiation is obtained. The visible peak splitting is due to incomplete monochromatization, which led to two diffraction peaks for $K_{\alpha1}$ and $K_{\alpha2}$, respectively. Additionally, due to the geometry of the liquid cell, the sample thickness could only be approximated roughly, leading to a slight shift in the peak baseline. Nevertheless, the obtained Bragg peaks match literature values for fcc gold.[72] Notably, the first indication of peaks related to gold is visible even after the first measurement, indicating that irradiation-induced gold reduction is not negligible during liquid-phase X-ray studies. This agrees with reports on X-ray-mediated gold reduction within minutes.[73]

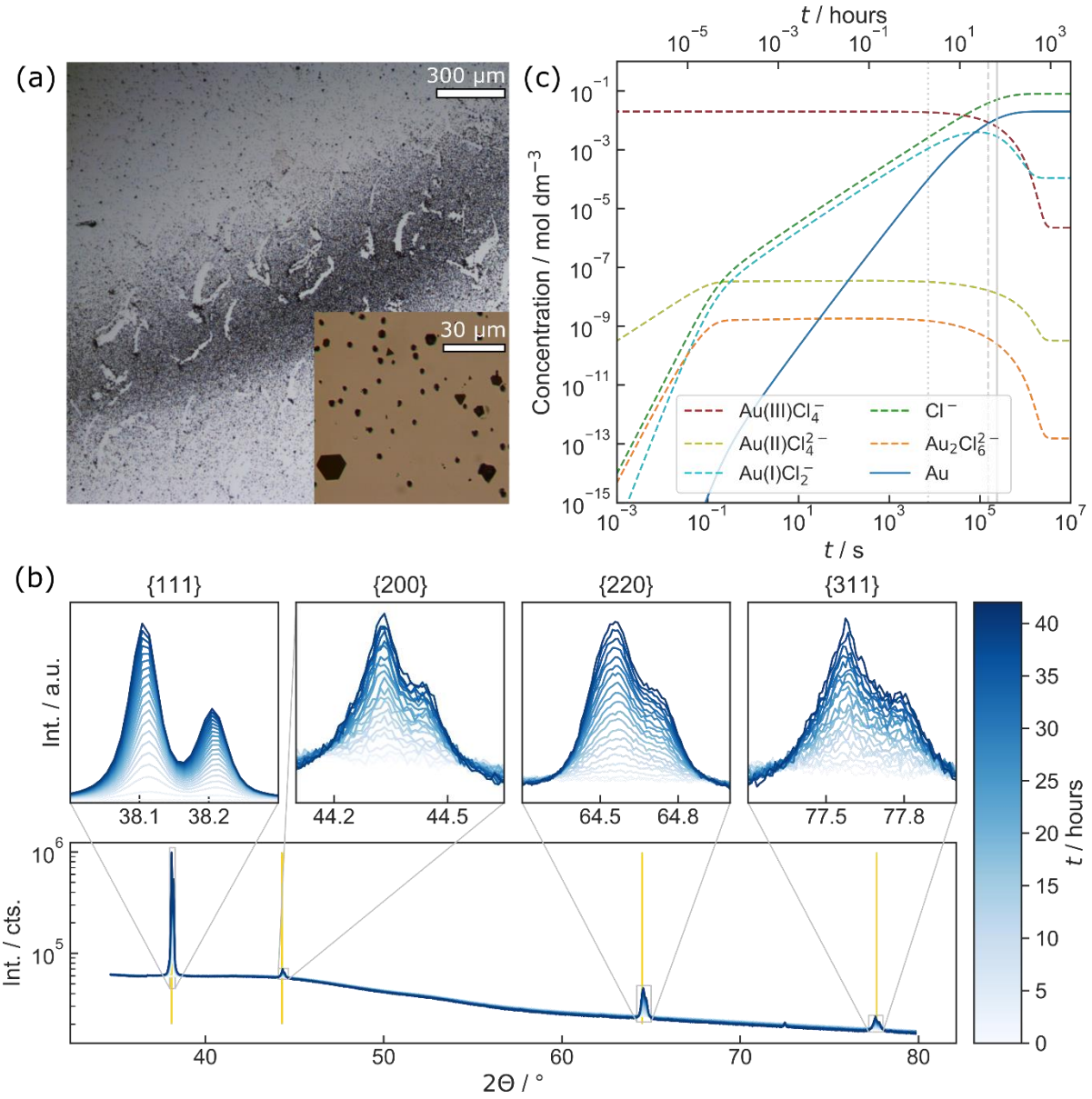


**Figure 4:** X-ray irradiation of a 20 mM HAuCl4-solution. (a) Optical micrographs showing micron-sized structures after 66 h of irradiation. The inset at higher resolution reveals that some form platelets of three- and sixfold symmetry, as expected for fcc-crystals. An *ex situ* XRD scan reveals that they consist of gold (**Figure S9(b)**). (b) *In situ* XRD investigation for 42 h in 2 h intervals at a dose rate of roughly 1 Gy $s^{-1}$. The vertical lines correspond to the lattice constant of gold[72]. (c) Corresponding kinetic simulation. For simplicity, only gold-containing species and $Cl^-$ are displayed. The grey lines mark the time after the first (2 h, dotted) and last *in situ* scan (42 h, dashed) experiment, as well as the time matching the experiment shown in (a) (66 h, solid).

**Figure *4(c)*** shows a corresponding kinetic simulation. While *g*-values precisely describing electron irradiation are available,[21] more general *g*-values acquired for low-linear energy transfer (LET) radiation such as photons are used here.[74] In contrast to kinetic simulations describing LP-TEM conditions, a steady-state condition is neither obtained within milliseconds

nor for the duration of the experiment. Instead, a constant increase of $Au^0$ over hours is expected until the system saturates in a steady state where almost all gold is reduced to pristine Au. As $Au^0$ is insoluble in water, it is expected to precipitate immediately. Furthermore, surfaces providing nucleation sites or seed crystals are known to support this process (heterogeneous nucleation). Thus, this simulation agrees with the constant increase in diffraction peak intensities presented in ***Figure 4(b)***.

These observations prove gold precipitation even when aqueous $HAuCl_4$ solutions are exposed to low dose rates, which is further indicated by gold reduction observed in photon-mediated radiolysis caused by lasing,[75,76] UV exposure,[77] or γ-irradiation,[54,59,60,78–81] at dose rates many orders of magnitude lower than those utilized in typical LP-TEM experiments. Moreover, the experimental findings demonstrate that beam effects must not be neglected for any experimental investigations of liquid phases using ionizing radiation even during low-dose exposure in standard laboratory conditions.

*3.2. Volatile species as radiolysis products*

It has been reported previously that nanobubbles in LP-TEM investigations of $HAuCl_4$ solutions can etch gold nanostructures.[32] It was concluded that this can only be related to reactive chlorine species within the gas phase, which can cause gold etching.[82] The high concentration of HCl predicted by the kinetic simulations performed within this work fits well with this observation, as HCl is known to be volatile. The formation of gaseous halide species has been reported for different ionizing radiations, as well.[83] It is noteworthy that this phenomenon appears regularly, as shown in ***Figure S10***. Here, a gold nanostructure is etched when directly contacting gas bubbles. If the gas bubble would mainly contain hydrogen, a passivation of the particle is expected to inhibit oxidative etching.[33]

In succession to etching, gold nanoparticles precipitate spatially isotropically in the vicinity of the gas bubbles (***Figure S10(b,c)***).[32] This is a strong indication of gaseous gold-containing

species, because only a gold-transfer mechanism *via* the gaseous phase explains the isotropic appearance of the gold particles beneath the bubble.[32] This fits well to the predicted formation of $Au_2Cl_6^{2-}$, as such structures have already been reported to exist in gas phase previously.[84] They could therefore cause such a nucleation behavior upon re-dissolution and supersaturation in the interfacing liquid.

### *3.3 Oxidative etching of gold nanostructures*

At both high dose rates and high concentrations, ***Figure 3*** reveals a dip in the relative $Au^0$ steady state concentration, in line with the increase of $Au_2Cl_6$ concentration. For 20 mM solutions, this is highlighted in ***Figure 5***. Here, the distribution of gold atoms within the main radiolysis products is again compared with the morphological findings of the evaluated experiments.

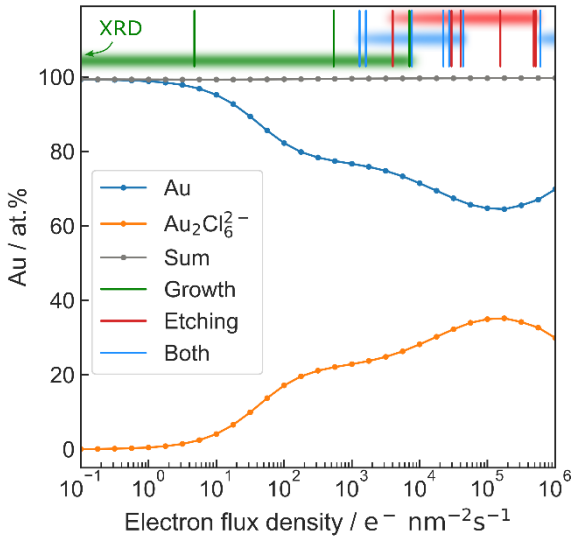


**Figure 5**: The steady state ratio of gold atoms distributed between the main radiolysis products $Au^0$ (dark-blue) and $Au_2Cl_6^{2-}$ (orange) of a 20 mM $HAuCl_4$ solution is plotted against the electron flux density. The two species store almost 100% of the gold atoms present (gray line). In addition, experiments performed within this work are marked with vertical lines and classified as growth (green), etching (red), or dynamics dominated by both processes (blue). The respective intervals are illustrated by shaded stripes.

Fifteen experimental observations were classified as either `growth' (green), `etching' (red), or `both' (blue), depending on the dominating phenomenon. While all growth events have been

observed at low-to-medium electron flux densities, etching events occur more often at larger dose rates. Experiments observing both mechanisms have been identified at medium-to-high electron flux densities.

The trend appears to follow the concentration of $Au^0$ shown in ***Figure 5***. However, as the electron flux density intervals of all three cases overlap, the different electron flux density regimes must not be understood as strict boundaries but should be regarded as a likelihood to observe the respective phenomenon. Naturally, the statistical information of only fifteen observations is limited. Therefore, no in-depth statistical analysis is performed on these inter-dependencies. Nevertheless, the trend indicated by the available data is in good agreement with the steady-state conditions predicted by our simulations.

The decrease of pristine Au at high electron flux densities shown in ***Figure 3*** and ***Figure 5*** appears only for (relatively) high initial $HAuCl_4$ concentrations. This verifies that oxidative etching of gold itself is a function of the initial $HAuCl_4$ concentration, as reported previously.[44] As illustrated in ***Figure 3***, this trend matches with our simulations, especially when a likely increase of concentration due to drying during the loading procedure is accounted for[69] (not shown in ***Figure 3***). Note that for the reported electron flux density ($> 10^7$ $e^-$ $nm^2s^{-1}$), our simulation predicts the conversion of a substantial amount of solvent to $H_2$, $O_2$, and $H_2O_2$. As Kim *et al.*[44] do not report any bubble formation, we assume that graphene membranes in the used graphene liquid cells significantly mitigate radiolysis effects due to their electrical conductivity. Hence, these experiments are noted at slightly reduced electron flux densities in ***Figure 3***.

The concentration dependency can be understood by the underlying chemistry: Gold reduction is mainly driven by solvated electrons ($e_h^-$) and H radicals[54] which are primary radiolysis products in aqueous solutions and thus are independent on the initial $HAuCl_4$ concentration. Gold oxidation, in turn, is suggested to occur *via* $ClOH^-$ as an oxidant.[37,38] In contrast to

primary radiolysis products, the formation of $ClOH^-$ strongly depends on the number of chlorine atoms available in the system, which is determined by the concentration of $HAuCl_4$.

At low $HAuCl_4$ concentrations, the amount of $ClOH^-$ is assumed to be insufficient to maintain a steady-state in which a substantial net $Au^0$ oxidation is notable. This hypothesis also agrees with studies showing a preferred gold etching in acidic environments at high (initial) chlorine concentrations[34,35] or demonstrating nucleation events at high dose rates, but low initial $HAuCl_4$ concentrations.[39] This is additionally demonstrated in the supporting information S6 (***Figure S14***).

In events combining growth and etching, these observations do not necessarily happen simultaneously but may show different temporal offsets, as shown in ***Figure S10*** and ***Figure S14***, as well as literature reports.[32,44,69] This can be understood when taking a closer look at the system itself. Our kinetic simulations assume a perfectly isotropic voxel, excluding phase boundaries or concentration gradients. Thus, steady-state concentrations are reached within a fraction of a second and without any transient behaviors. However, concentration gradients and heterogeneous phase compositions are expected to delay this process, shifting it to observable time scales and causing transients. In other words: only surface atoms of a nanostructure can contribute to a chemical reaction, whereas interior atoms remain passive.

Therefore, the system can be analyzed best at an experiment showing a slow response of the particles to mitigate the effect of steep overshoots or oscillations. ***Figure 6(a)*** shows micrographs of the temporal evolution of a gold nanostructure in LP-TEM. The particle was present before electron irradiation and is thus regarded as a charge-dissipation product caused by the graphene membrane (see supplement, section S4 for details[26,27,85–88]).

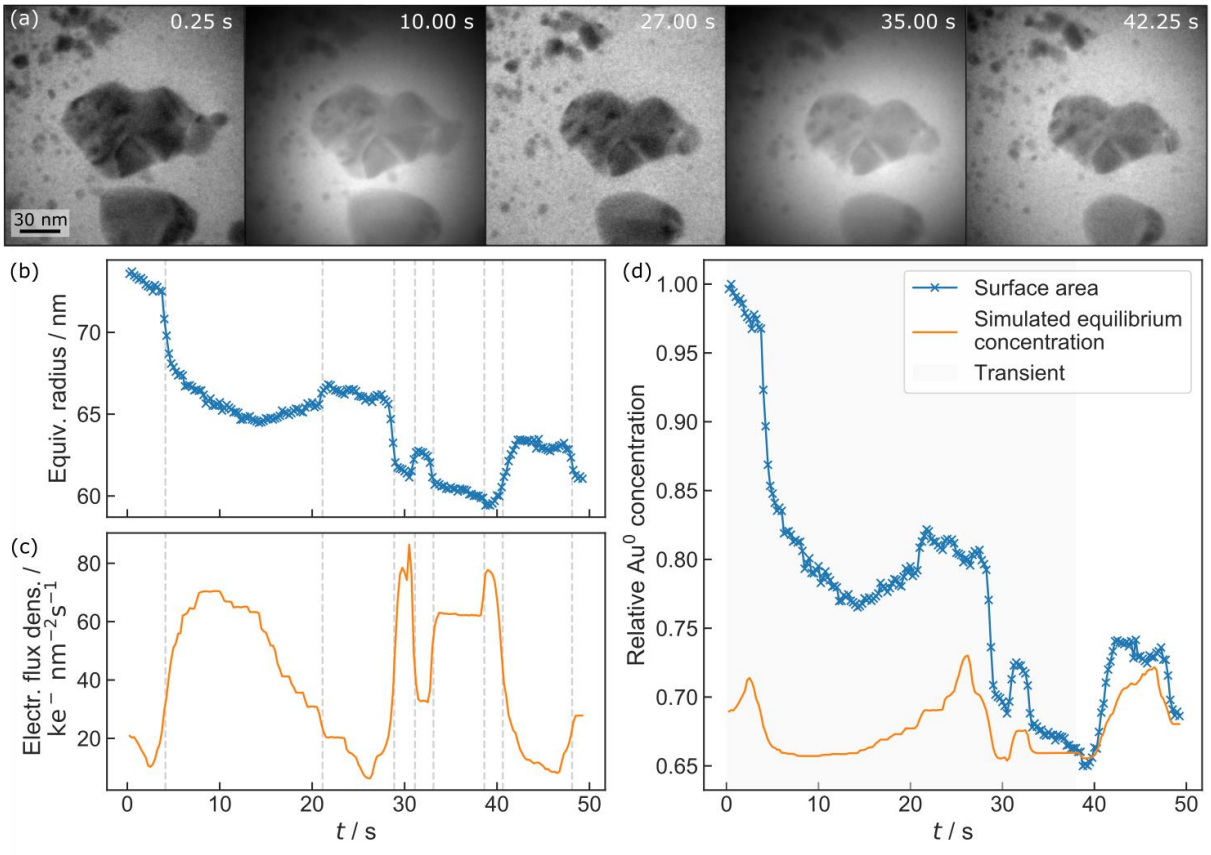


**Figure 6: (**a) Series of bright-field TEM micrographs showcasing the evolution of a gold nanostructure in 20 mM $HAuCl_4$ solution under repetitive *in situ* beam contraction. (b) The evolution of the equivalent radius for the centred particle in (a) is directly related to the electron flux density (c). It is evident that the inflection points in (b) and (c) coincide. (d) The relative steady-state concentrations of Au and the relative evolution of the equivalent spherical surface area describing the centred particle in (a) is displayed.

The nanostructure is exposed to repetitive beam contraction. Consequently, the dose rate is enhanced locally, altering the redox chemistry. By assuming a spherical geometry, the particle size can be tracked by a single parameter,[1] describing the sphere's radius with a cross sectional area equivalent to the projected particle size. This equivalent radius is plotted in ***Figure 6(b)***. Its temporal evolution appears to be highly correlated with the applied electron flux density ***Figure 6(c)***). Their points of inflection coincide, as indicated by the gray-shaded, dotted lines. Thus, the gold reduction/oxidation process immediately responds to abrupt changes in local dose rate, in accordance with the rapid steady-state formation in the kinetic simulations.

This is further investigated by translating the electron flux density to the amount of reduced gold by describing the electron flux density range of interest with a polynomial of third order (***Figure S13***).

To compare this with experimental data, the equivalent spherical surface area with a cross-section matching with the initial particle reflects the amount of $Au^0$ available in the observed volume. Its initial value is assumed to correspond to the maximum value of gold surface atoms available because this would coincide with the irradiation at low electron flux densities.

As shown in ***Figure 6(d)***, it is evident that simulation and measurement show a large offset that decays until about 38 s after which both plots converge (see shaded area in ***Figure 6(d)***). The transients may cause the offset. In addition, the two curve shapes increase in similarity until they show consistent features. This is regarded as a strong indication of the quantitative validity of the simulated model.

*3.4. Implications of dose rate dependency on redox chemistry and Gibbs free energy landscape*

By adjustment of the experimental conditions in combination with fitting of the dose rate, the Gibbs free energy landscape can be tailored. This is herein probed by investigating the stability of gold nanoparticles.

As elucidated previously, classical nucleation theory does not fully describe nucleation of nanostructures because it does not cover so-called non-classical nucleation pathways like e.g. formation via cluster clouds[12,13]. However, it provides reliable information on the minimum size at which a nanostructure can be regarded as stable. This is quantified by the critical radius $r_{crit}$, which is reliably accessible during nanoparticle dissolution or etching[31]. It is defined by the Gibbs free surface energy $\gamma$, the atomic volume $\Omega$, and the difference in the chemical potential between the initial and the final phase under equilibrium conditions $\Delta\mu$.[89]

$$r_{crit} = \frac{2\gamma\Omega}{\Delta\mu} \qquad (2)$$

Under similar experimental conditions, the thermal energy $k_B T$ (with $k_B$ being the Boltzmann constant) remains constant. Thus, $\Delta\mu$ is governed by the changes in substance (see supporting information, section S7 for details):[89,90]

$$\Delta\mu = k_B T \ln\left(\frac{c_0(HAuCl_4)}{c_{steady\ state}(Au^0)}\right) \quad (3)$$

This natural logarithm is plotted in ***Figure 7(a)*** as a function of electron flux density, showing a significant increase with $c_0$ under high electron flux densities. According to equation (*2*), this correlates with an expected decrease in $r_{crit}$.

The described behavior was investigated by measuring $r_{crit}$ of 17 different nanoparticles at three different initial concentrations of $HAuCl_4$ (7 at 1 mM, 3 at 10 mM, and 7 at 20 mM). $r_{crit}$ was obtained by analyzing the slope of the etching rate (see the supplementary information S7 for details[31,91,92]). All experiments were conducted at electron flux densities of the same order of magnitude ($1.6 – 6.1 \cdot 10^5$ $e^-$ $(nm^2 s)^{-1}$). As shown by the shaded region in ***Figure 7(a)***, the effect of these variations on the chemical potential is small compared to the influence of $c_0$. The resulting critical radii are plotted in ***Figure 7(b)*** dependent on the initial $HAuCl_4$ concentration. The obtained critical radii scatter stronger at lower $c_0$, emphasizing that $r_{crit}$ is heavily affected by stochastic processes. Nevertheless, the reduction in scattering with $c_0$ is an initial indicator for a dominating influence of $c_0$, which is even more pronounced when following the respective mean values. Here, a significant reduction of $r_{crit}$ is observed with increasing initial chloride concentration, as predicted by the relative changes in the radiochemistry. The relative change amounting to a factor of two between 1 mM and 20 mM $HAuCl_4$ solutions is well matched by differences in $\Delta\mu$ depicted in ***Figure 7(a)***.

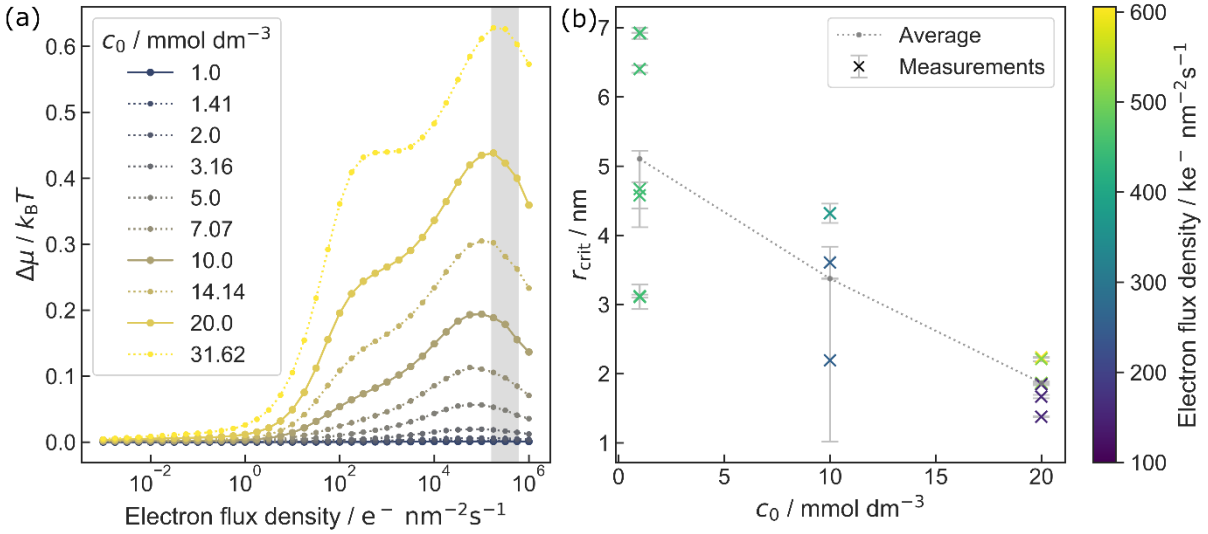


**Figure 7**: (a) Chemical potential in units of $k_BT$, corresponding to the natural logarithm of the initial $HAuCl_4$ concentration and the steady state concentration of $Au^0$ as a function of the electron flux density. The shaded area and solid lines relate to the data relevant to (b). (b) $r_{crit}$ for different initial concentrations of $HAuCl_4$ solutions are shown. The gray-shaded data correspond to the respective average of 5.1, 3.4, and 1.9 nm for 1, 10, and 20 mM solutions of $HAuCl_4$, respectively. The color bar depicts the electron flux density during the experiment. The error bars denote the precision of the least-squares optimization (see supplementary information, section S7 for details).

At 1 mM, ***Figure 7(a)*** suggests no significant difference in chemical potential, as the steady-state mol fraction of $Au^0$ is expected to amount to 1 here (***Figure 3***). Consequently, the transitions observed are expected to be reversible. Hence, the state can be interpreted as a dynamic equilibrium. This is in line with the experimental findings in ***Figure S14*** showing reversible growth and dissolution. Furthermore, at 1 mM the average value of $r_{crit}$ is in the same range as values obtained for Pt-nanoparticles in 0.228 M $FeCl_3$ aqueous solution.[31]

The reversible process is still driven by the electron beam, because it defines the dynamic equilibrium condition itself (i.e. by changing the solution chemistry). However, this suggests that such dynamic equilibria could be well-suited for analyzing material-specific parameters.

Besides, a decrease in the Gibbs free surface energy $\gamma$ would relate to a smaller $r_{crit}$ (equation (3)). However, gold surfaces are highly stabilized by chloride.[93] Although the relative concentration of $Cl^-$ decreases with the initial $HAuCl_4$ concentration at the electron flux density range of interest, the absolute concentration still increases. Consequently, the gold surface is

considered to remain saturated with $Cl^-$ in all conducted experiments, and, thus, changes in $\gamma$ are expected to be negligible.

## 4. Conclusion

We introduce an automated tool to simulate kinetic models for radiation-defined redox chemistries in liquid environments, allowing for a facile simulation of complex models. This is demonstrated for the reduction of aqueous $HAuCl_4$ solutions, showing good agreement with experimental findings using LP-TEM, *in situ* XRD, and literature data. Our findings emphasize that accurate and holistic modeling of beam effects is not only necessary but allows for drawing meaningful conclusions for unbiased (i.e., not irradiated) systems, even when operating at high dose rates.

## 5. Experimental Section/Methods

Experiments were conducted using a GSMLC with a well depth of 100 nm and a Philipps CM30 (S)TEM in TEM mode, and a frame rate of 4 frames per second. Liquid encapsulation was performed using 6 — 8 layer trivial-transfer graphene (ACS Material) transferred onto holey carbon-coated gold TEM grids (Quantifoil, PLANO). Fabrication and handling of GSMLCs have been elucidated elsewhere.[47,69] Experiments at 1 mM $HAuCl_4$ solution and electron flux densities below $10^4$ $e^-$ $(nm^2s)^{-1}$ were conducted using a Protochips Poseidon Select E-Chip and a Thermo Fisher Scientific (formerly FEI) Titan³ Themis 80-300 (S)TEM. Both microscopes were operated at an acceleration voltage of 300 kV. All silicon nitride membranes were plasma treated prior to filling using ambient air plasma. Crystalline $HAuCl_4 \cdot 3\ H_2O$ (Alpha Aeasar) was dissolved in de-ionized water as a specimen solution. Data curation of TEM experiments was performed using FIJI.[94]

XRD measurements were conducted with a Rigaku Smart-Lab diffractometer using a Hypix 3000 solid-state 2D detector. The Cu-rotating anode X-ray source was operated with an

acceleration voltage of 45 kV and a current of 160 mA on the Wolfram filament. The X-ray spectrum was not monochromatized to increase primary beam intensity. 5-degree Soller slits were used on the incident and receiving optics. The incident slit was opened completely, resulting in a 7x15 mm beam. Both receiving slits were closed down to 0.2 mm. Measurements and irradiation were carried out in Bragg-Brentano geometry. The liquid cell containing aqueous 20 mM $HAuCl_4$ solution was lying flat in the goniometer center and was irradiated for about 1.75 h in between the *in situ* XRD scans. After the irradiation step, a 20 minute $\theta/2\theta$-scan from 35 ° to 80 ° was performed to record the developing Bragg peaks of the nucleated gold particles. Irradiation and measurement were repeated 21 times, resulting in a total measurement time of 42 h.

**Author contribution**

**Birk Fritsch:** Writing – original draft (lead), data curation (lead), Investigations (equal) – LP-TEM at 20 mM (lead), 1 mM (supporting), formal analysis (lead), Software (lead) – Radiolysis tool (lead), GUI (supporting), Graph analysis (lead), Methodology (lead), Review and editing (lead).
**Tobias Zech:** Investigations (supporting) – XRD-Studies (lead), Formal analysis – (supporting), Writing – original draft (supporting), Review and editing (supporting)
Mark Bruns: Investigations (supporting) – Electrochemical studies (lead), Writing – original draft (supporting), Review and editing (supporting).
**Andreas Körner**: Software (supporting) – Graph analysis (supporting), Radiolysis tool (supporting) – code review, Validation –, Formal analysis (supporting) – Graph analysis (supporting), Writing – original draft (supporting), Formal analysis – (supporting), Review and editing (supporting).
**Saba Khadivianazar:** Software (supporting) – Radiolysis tool (supporting), Validation (supporting) – Verification against Matlab simulations (lead), Review and editing (supporting).
**Mingjian Wu:** Investigations (supporting) – LP-TEM at 1 mM (equal), Review and editing (supporting).
**Neda Zargar Talebi:** Software (supporting) – GUI (lead), Graph analysis (supporting), Review and editing (supporting)**.**
**Sannakaisa Virtanen**: Supervision (supporting), Review and editing (supporting), Project Administration, Funding Acquisition (supporting).
**Tobias Unruh**: Supervision (supporting), Review and editing (supporting), Project Administration, Funding Acquisition (supporting).
**Michael P.M. Jank**: Conceptualization (supporting), Supervision (equal), Review and editing (supporting), Project Administration (equal), Methodology (supporting), Funding Acquisition (supporting).

**Erdmann Spiecker**: Conceptualization (supporting), Supervision (equal), Project Administration (equal), Methodology (supporting), Review and editing (supporting), Funding Acquisition (lead).
**Andreas Hutzler**: Investigations (equal) – LP-TEM at 1 mM (equal), LP-TEM at 10 mM (lead), Data curation (supporting), Methodology (supporting), Conceptualization (lead), Review and editing (supporting), Supervision (equal), Project Administration, Funding Acquisition (supporting).

## Supporting Information

Supporting Information is available from ChemRxiv or from the authors.

## Acknowledgements

Financial support by the German Research Foundation (DFG) *via* the Research Training Group GRK 1896 "*In situ* microscopy with electrons, X-rays and scanning probes" (218975129), the Cluster of Excellence "Engineering of Advanced Materials (EAM)" (53244630), the research group FOR 1878 "funCOS - Functional Molecular Structures on Complex Oxide Surfaces" (214951840), the collaborative research center SFB 1452 "Catalysis at Liquid Interfaces (CLINT)" (431791331) is gratefully acknowledged. Financial support by the German Federal Ministry of Education and Research (BMBF) *via* the project 05K16WE1 is gratefully acknowledged.

## References

[1] M. M. Modena, B. Rühle, T. P. Burg, S. Wuttke, *Advanced materials (Deerfield Beach, Fla.)* **2019**, *31*, e1901556.
[2] A. S. Kashin, V. P. Ananikov, *Nat Rev Chem* **2019**, *3*, 624.
[3] Y. Yuan, M. Li, Z. Bai, G. Jiang, B. Liu, T. Wu, Z. Chen, K. Amine, J. Lu, *Advanced Materials* **2019**, *31*, e1805609.
[4] Z.-W. Yin, S. B. Betzler, T. Sheng, Q. Zhang, X. Peng, J. Shangguan, K. C. Bustillo, J.-T. Li, S.-G. Sun, H. Zheng, *Nano Energy* **2019**, *62*, 507.
[5] Z. Fan, L. Zhang, D. Baumann, L. Mei, Y. Yao, X. Duan, Y. Shi, J. Huang, Y. Huang, X. Duan, *Advanced Materials* **2019**, *31*, e1900608.
[6] X. Zhang, W. Liu, Z. Chen, Y. Huang, W. Liu, Y. Yu, *Adv Energy Sustain Res* **2021**.
[7] G. Rong, X. Zhang, W. Zhao, Y. Qiu, M. Liu, F. Ye, Y. Xu, J. Chen, Y. Hou, W. Li, W. Duan, Y. Zhang, *Advanced Materials* **2017**, *29*, 1606187.
[8] H. Wu, H. Friedrich, J. P. Patterson, Sommerdijk, Nico A. J. M., N. de Jonge, *Advanced materials (Deerfield Beach, Fla.)* **2020**, *32*, e2001582.
[9] J. J. de Yoreo, S. N. A. J. M., *Nat Rev Mater* **2016**, *1*, 16041.
[10] W. J. Dearnaley, B. Schleupner, A. C. Varano, N. A. Alden, F. Gonzalez, M. A. Casasanta, B. E. Scharf, M. J. Dukes, D. F. Kelly, *Nano Letters* **2019**, *19*, 6734.
[11] G. M. Jonaid, W. J. Dearnaley, M. A. Casasanta, L. Kaylor, S. Berry, M. J. Dukes, M. S. Spilman, J. L. Gray, D. F. Kelly, *Advanced Materials* **2021**, *33*, e2103221.

[12] B. Jin, Y. Wang, Z. Liu, A. France-Lanord, J. C. Grossman, C. Jin, R. Tang, *Advanced materials (Deerfield Beach, Fla.)* **2019**, *31*, e1808225.
[13] N. D. Loh, S. Sen, M. Bosman, S. F. Tan, J. Zhong, C. A. Nijhuis, P. Král, P. Matsudaira, U. Mirsaidov, *Nature Chemistry* **2017**, *9*, 77.
[14] A. Ianiro, H. Wu, M. M. J. van Rijt, M. P. Vena, A. D. A. Keizer, A. C. C. Esteves, R. Tuinier, H. Friedrich, Sommerdijk, Nico A. J. M., J. P. Patterson, *Nature Chemistry* **2019**, *11*, 320.
[15] A. Bo, Y. Liu, B. Kuttich, T. Kraus, A. Widmer-Cooper, N. de Jonge, *Advanced Materials* **2022**.
[16] N. Jiang, *Ultramicroscopy* **2017**, *179*, 81.
[17] U. Mirsaidov, J. P. Patterson, H. Zheng, *MRS Bull.* **2020**, *45*, 704.
[18] B. Fritsch, A. Hutzler, M. Wu, S. Khadivianazar, L. Vogl, M. P. M. Jank, M. März, E. Spiecker, *Nanoscale Adv.* **2021**, *3*, 2466.
[19] T.-H. Hsieh, J.-Y. Chen, C.-W. Huang, W.-W. Wu, *Chem. Mater.* **2016**, *28*, 4507.
[20] C. Wang, T. Shokuhfar, R. F. Klie, *Advanced Materials* **2016**, *28*, 7716.
[21] N. M. Schneider, M. M. Norton, B. J. Mendel, J. M. Grogan, F. M. Ross, H. H. Bau, *J. Phys. Chem. C* **2014**, *118*, 22373.
[22] T. J. Woehl, P. Abellan, *Journal of microscopy* **2017**, *265*, 135.
[23] M. Wang, C. Park, T. J. Woehl, *Chem. Mater.* **2018**, *30*, 7727.
[24] J. Korpanty, L. R. Parent, N. C. Gianneschi, *Nano Letters* **2021**, *21*, 1141.
[25] J. R. Jokisaari, X. Hu, A. Mukherjee, V. Uskoković, R. F. Klie, *Nanotechnology* **2021**, *32*, 485707.
[26] S. Keskin, N. de Jonge, *Nano Letters* **2018**, *18*, 7435.
[27] H. Cho, M. R. Jones, S. C. Nguyen, M. R. Hauwiller, A. Zettl, A. P. Alivisatos, *Nano Letters* **2017**, *17*, 414.
[28] A. Khelfa, J. Nelayah, H. Amara, G. Wang, C. Ricolleau, D. Alloyeau, *Advanced Materials* **2021**, *33*, e2102514.
[29] K. Lim, Y. Bae, S. Jeon, K. Kim, B. H. Kim, J. Kim, S. Kang, T. Heo, J. Park, W. C. Lee, *Advanced materials (Deerfield Beach, Fla.)* **2020**, *32*, e2002889.
[30] D. Keller, T. R. Henninen, R. Erni, *Nanoscale* **2020**, *12*, 22511.
[31] Y. Jiang, G. Zhu, G. Dong, F. Lin, H. Zhang, J. Yuan, Z. Zhang, C. Jin, *Micron (Oxford, England 1993)* **2017**, *97*, 22.
[32] A. Hutzler, B. Fritsch, M. P. M. Jank, R. Branscheid, R. C. Martens, E. Spiecker, M. März, *Adv. Mater. Interfaces* **2019**, *6*, 1901027.
[33] M. R. Hauwiller, J. C. Ondry, C. M. Chan, P. Khandekar, J. Yu, A. P. Alivisatos, *Journal of the American Chemical Society* **2019**, *141*, 4428.
[34] A. Khelfa, J. Meng, C. Byun, G. Wang, J. Nelayah, C. Ricolleau, H. Amara, H. Guesmi, D. Alloyeau, *Nanoscale* **2020**, *12*, 22658.
[35] J. Hermannsdörfer, N. de Jonge, A. Verch, *Chemical communications (Cambridge, England)* **2015**, *51*, 16393.
[36] W. Bras, D. A. A. Myles, R. Felici, *Journal of physics. Condensed matter an Institute of Physics journal* **2021**, *33*, 423002.
[37] J. H. Park, N. M. Schneider, J. M. Grogan, M. C. Reuter, H. H. Bau, S. Kodambaka, F. M. Ross, *Nano Letters* **2015**, *15*, 5314.
[38] B. Ambrožič, A. Prašnikar, N. Hodnik, N. Kostevšek, B. Likozar, K. Ž. Rožman, S. Šturm, *Chemical science* **2019**, *10*, 8735.
[39] B. Jin, M. L. Sushko, Z. Liu, C. Jin, R. Tang, *Nano Letters* **2018**, *18*, 6551.
[40] X. Ma, F. Lin, X. Chen, C. Jin, *ACS nano* **2020**, *14*, 9594.
[41] Y. Zhang, D. Keller, M. D. Rossell, R. Erni, *Chem. Mater.* **2017**, *29*, 10518.
[42] W.-G. Jung, J. H. Park, Y.-R. Jo, B.-J. Kim, *Journal of the American Chemical Society* **2019**, *141*, 12601.

[43] P. M. G. Deursen, R. I. Koning, V. Tudor, M.-A. Moradi, J. P. Patterson, A. Kros, Sommerdijk, Nico A. J. M., A. J. Koster, G. F. Schneider, *Advanced Functional Materials* **2020**, *30*, 1904468.
[44] S. Y. Kim, K. S. Dae, K. Koo, D. Kim, J. Park, J. M. Yuk, *Phys. Status Solidi A* **2019**, *216*, 1800949.
[45] D. Alloyeau, W. Dachraoui, Y. Javed, H. Belkahla, G. Wang, H. Lecoq, S. Ammar, O. Ersen, A. Wisnet, F. Gazeau, C. Ricolleau, *Nano Letters* **2015**, *15*, 2574.
[46] B. Jin, H. Wang, M. L. Sushko, C. Jin, R. Tang, *Nanoscale* **2020**, *12*, 19592.
[47] A. Hutzler, T. Schmutzler, M. P. M. Jank, R. Branscheid, T. Unruh, E. Spiecker, L. Frey, *Nano Letters* **2018**, *18*, 7222.
[48] C. R. Harris, K. J. Millman, S. J. van der Walt, R. Gommers, P. Virtanen, D. Cournapeau, E. Wieser, J. Taylor, S. Berg, N. J. Smith, R. Kern, M. Picus, S. Hoyer, M. H. van Kerkwijk, M. Brett, A. Haldane, J. F. Del Río, M. Wiebe, P. Peterson, P. Gérard-Marchant, K. Sheppard, T. Reddy, W. Weckesser, H. Abbasi, C. Gohlke, T. E. Oliphant, *Nature* **2020**, *585*, 357.
[49] J. D. Hunter, *Comput. Sci. Eng.* **2007**, *9*, 90.
[50] W. McKinney, in *Proceedings of the 9th Python in Science Conference*, SciPy **2010**, p. 56.
[51] P. Virtanen, R. Gommers, T. E. Oliphant, M. Haberland, T. Reddy, D. Cournapeau, E. Burovski, P. Peterson, W. Weckesser, J. Bright, S. J. van der Walt, M. Brett, J. Wilson, K. J. Millman, N. Mayorov, A. R. J. Nelson, E. Jones, R. Kern, E. Larson, C. J. Carey, İ. Polat, Y. Feng, E. W. Moore, J. VanderPlas, D. Laxalde, J. Perktold, R. Cimrman, I. Henriksen, E. A. Quintero, C. R. Harris, A. M. Archibald, A. H. Ribeiro, F. Pedregosa, P. van Mulbregt, *Nat Methods* **2020**, *17*, 261.
[52] M. N. Yesibolati, S. Laganá, S. Kadkhodazadeh, E. K. Mikkelsen, H. Sun, T. Kasama, O. Hansen, N. J. Zaluzec, K. Mølhave, *Nanoscale* **2020**, *12*, 20649.
[53] S. Seltzer, *Stopping-Powers and Range Tables for Electrons, Protons, and Helium Ions, NIST Standard Reference Database 124*, National Institute of Standards and Technology **1993**.
[54] G. R. Dey, A. K. El Omar, J. A. Jacob, M. Mostafavi, J. Belloni, *J. Phys. Chem. A* **2011**, *115*, 383.
[55] U. K. Kläning, K. Sehested, T. Wolff, *J. Chem. Soc., Faraday Trans. 1* **1984**, *80*, 2969.
[56] U. K. Klaning, K. Sehested, J. Holcman, *J. Phys. Chem.* **1985**, *89*, 760.
[57] M. Kelm, E. Bohnert, *A kinetic model for the radiolysis of chloride brine, its sensitivity against model parameters and a comparison with experiments: Wissenschaftliche Berichte FZKA 6977*, Karlsruhe, Karlsruhe **2004**.
[58] A. V. Levanov, O. Y. Isaikina, *Ind. Eng. Chem. Res.* **2020**, *59*, 14278.
[59] G. V. Buxton, R. M. Sellers, *Coordination Chemistry Reviews* **1977**, *22*, 195.
[60] E. Gachard, H. Remita, J. Khatouri, B. Keita, L. Nadjo, a. J. Belloni, *New J. Chem.* **1998**, *22*, 1257.
[61] K. Sehested, H. Corfitzen, J. Holcman, E. J. Hart, *J. Phys. Chem.* **1992**, *96*, 1005.
[62] M. C. Sauer, W. G. Brown, E. J. Hart, *J. Phys. Chem.* **1984**, *88*, 1398.
[63] S. Sunder, H. Christensen, *Nuclear Technology* **1993**, *104*, 403.
[64] A. Trummal, L. Lipping, I. Kaljurand, I. A. Koppel, I. Leito, *J. Phys. Chem. A* **2016**, *120*, 3663.
[65] D. Wu, D. Wong, B. Di Bartolo, *Journal of Photochemistry* **1980**, *14*, 303.
[66] R. C. Dunn, J. D. Simon, *J. Am. Chem. Soc.* **1992**, *114*, 4856.
[67] A. A. Hagberg, D. A. Schult, P. J. Swart, in *Proceedings of the 7th Python in Science conference (SciPy 2008)*, Vol. 1 (Eds.: G. Varoquaux, T. Vaught, J. Millman) **2008**, p. 11.

[68] T. D. Holmes, R. H. Rothman, W. B. Zimmerman, *Plasma Chem Plasma Process* **2021**, *41*, 531.
[69] A. Hutzler, B. Fritsch, M. P. M. Jank, R. Branscheid, E. Spiecker, M. März, *Journal of visualized experiments: JoVE* **2019**.
[70] Y. Bae, S. Kang, B. H. Kim, K. Lim, S. Jeon, S. Shim, W. C. Lee, J. Park, *Engineering* **2021**, *7*, 630.
[71] S. Keskin, C. Pawell, N. de Jonge, *Micron* **2021**, *149*, 103109.
[72] B. N. Dutta, B. Dayal, *Phys. Status Solidi B* **1963**, *3*, 473.
[73] A. Plech, V. Kotaidis, A. Siems, M. Sztucki, *Physical chemistry chemical physics PCCP* **2008**, *10*, 3888.
[74] B. Pastina, J. A. LaVerne, *J. Phys. Chem. A* **2001**, *105*, 9316.
[75] N. I. Smith, K. Mochizuki, H. Niioka, S. Ichikawa, N. Pavillon, A. J. Hobro, J. Ando, K. Fujita, Y. Kumagai, *Nature Communications* **2014**, *5*, 5144.
[76] F. Sahebi, M. Ranjbar, M. T. Goodarzi, *Appl. Phys. A* **2019**, *125*.
[77] Y. Shang, C. Min, J. Hu, T. Wang, H. Liu, Y. Hu, *Solid State Sciences* **2013**, *15*, 17.
[78] L. Freitas de Freitas, G. H. C. Varca, J. G. Dos Santos Batista, A. Benévolo Lugão, *Nanomaterials (Basel, Switzerland)* **2018**, *8*.
[79] J. Belloni, J.-L. Marignier, M. Mostafavi, *Radiation Physics and Chemistry* **2020**, *169*, 107952.
[80] H. Ki, S. Park, S. Eom, J. Gu, S. Kim, C. Kim, C. W. Ahn, M. Choi, S. Ahn, D.-S. Ahn, J. Choi, M.-H. Baik, H. Ihee, *International journal of molecular sciences* **2020**, *21*.
[81] M. Toro-González, D. M. Clifford, M. C. Molina, C. E. Castano, J. V. Rojas, *Radiation Physics and Chemistry* **2021**, *188*, 109614.
[82] S. King, J. Massicot, A. McDonagh, *Metals* **2015**, *5*, 1454.
[83] N. K. Richards-Henderson, K. M. Callahan, P. Nissenson, N. Nishino, D. J. Tobias, B. J. Finlayson-Pitts, *Phys. Chem. Chem. Phys.* **2013**, *15*, 17636.
[84] L. Nalbandian, S. Boghosian, G. N. Papatheodorou, *Inorg. Chem.* **1992**, *31*, 1769.
[85] S. Hettler, E. Kano, M. Dries, D. Gerthsen, L. Pfaffmann, M. Bruns, M. Beleggia, M. Malac, *Ultramicroscopy* **2018**, *184*, 252.
[86] S. Hettler, J. Onoda, R. Wolkow, J. Pitters, M. Malac, *Ultramicroscopy* **2019**, *196*, 161.
[87] S. Sinha, J. H. Warner, *Small Structures* **2021**, *2*, 2000049.
[88] J. M. Grogan, N. M. Schneider, F. M. Ross, H. H. Bau, *Nano Letters* **2014**, *14*, 359.
[89] C. N. Nanev, in *Handbook of crystal growth* (Eds.: T. Nishinga, T. F. Kuech, P. Rudolph), Elsevier. Amsterdam **2015**, p. 315.
[90] H. A. Vinutha, D. Frenkel, *The Journal of Chemical Physics* **2021**, *154*, 124502.
[91] R. J. Seager, A. J. Acevedo, F. Spill, M. H. Zaman, *Sci Rep* **2018**, *8*, 7711.
[92] Y. Hattori, Y. Haruna, M. Otsuka, *Colloids and surfaces. B, Biointerfaces* **2013**, *102*, 227.
[93] S. Gómez-Graña, B. Goris, T. Altantzis, C. Fernández-López, E. Carbó-Argibay, A. Guerrero-Martínez, N. Almora-Barrios, N. López, I. Pastoriza-Santos, J. Pérez-Juste, S. Bals, G. van Tendeloo, L. M. Liz-Marzán, *J. Phys. Chem. Lett.* **2013**, *4*, 2209.
[94] J. Schindelin, I. Arganda-Carreras, E. Frise, V. Kaynig, M. Longair, T. Pietzsch, S. Preibisch, C. Rueden, S. Saalfeld, B. Schmid, J.-Y. Tinevez, D. J. White, V. Hartenstein, K. Eliceiri, P. Tomancak, A. Cardona, *Nature Methods* **2012**, *9*, 676.